ChemComm

COMMUNICATION

View Article Online
View Journal | View Issue

Cite this: *Chem. Commun.*, 2017, 53, 2044

Received 26th November 2016,
Accepted 16th January 2017

DOI: 10.1039/c6cc09442b

rsc.li/chemcomm

Coupling multiphase-Fe and hierarchical N-doped graphitic carbon as trifunctional electrocatalysts by supramolecular preorganization of precursors†

Zhixin Zhou,[a] Fei He,[a] Yanfei Shen,[b] Xinghua Chen,[a] Yiran Yang,[a] Songqin Liu,[a] Toshiyuki Mori[c] and Yuanjian Zhang*[a]

A hydrogen bond-driven supramolecular strategy to synthesize multiphase-Fe anchoring on hierarchical N-doped graphitic carbon was proposed. As a result, the as-obtained catalysts showed unusual trifunctional activities in the oxygen reduction reaction, oxygen evolution reaction and hydrogen evolution reaction, even surpassing noble-metal catalysts such as Pt/C and RuO_2.

Molecular assembly is the formation of stable aggregates with a well-defined composition and structure under equilibrium conditions, based on non-covalent interactions among molecules.[1] For example, as typical coordination-driven assemblies, metal–organic frameworks (MOFs) that simultaneously display both porosity and a highly tailorable structure have attracted considerable attention.[2] The atom-level control over molecular and supramolecular structures afforded by MOFs have emerged recently as a new platform for the synthesis of carbon-based materials,[2a] which show great promise as nonprecious metal catalysts to replace noble metals (*e.g.* Pt, IrO_2 and RuO_2) in the oxygen reduction reaction (ORR),[3] oxygen evolution reaction (OER)[3a,b,d] and hydrogen evolution reaction (HER).[2b] However, the thermal transformation of MOFs into electrocatalysts usually suffers from the breakdown inside the MOF crystal owing to their inherent microporous structure.[2a,3b,c] Thus, MOF-derived materials are mostly microporous and show a poor degree of graphitization, both of which are considered unfavorable for high-performance electrocatalytic processes.[3b,c] Moreover, to obtain regular porous structures, organic ligands of MOFs need to be specially designed, which hampers the large-scale application from the point of view of economy and sustainability.[3d] Therefore, the development of a highly efficient assembly strategy for the synthesis of electrocatalysts with favorable structures is highly desired for electrocatalysis, but remains a challenge.

Nature has evolved hydrogen bonds among molecules as an important recognition strategy to execute most of the biological processes.[1b] Indeed, as hydrogen bond has strong direction, reversibility, and specificity, hydrogen bond-driven assembly could form ordered and close-packed crystalline structures, which would provide an alternative method to prepare carbon-based materials with well-defined morphologies and structures.[1a] Very recently, self-assembled supramolecular precursors by hydrogen bonds enabled the synthesis of hierarchical graphitic carbon nitride with improved photocatalytic activities.[1a,4] However, hydrogen bond-driven assembly-derived electrocatalysts have been rarely exploited.

Herein, we report that an ordered and close-packed crystal composed of low-cost barbituric acid (BA), 2,4,6-triaminopyrimidine (TAP) and $FeCl_3$ obtained *via* hydrogen bond-driven supramolecular assembling (Fig. 1a) could be pyrolyzed into multiphase-Fe anchoring on hierarchical N-doped graphitic carbon, without the unwanted collapse of the structure that MOF precursors often encountered. In contrast, the control samples that were prepared without the supramolecular approach could not achieve this unique structure. Consequently, the as-obtained catalyst exclusively exhibited competitive ORR, OER and HER activities with respect to Pt/C and RuO_2, making it an unusual trifunctional non-precious electrocatalyst.

Two C and N containing compounds, *i.e.*, BA and TAP, were deliberately chosen as precursors as they could form up to three stable hydrogen bonds (denoted BA–TAP, see Fig. S1, ESI†).[1a,4a] Simultaneously, $FeCl_3$ could be adsorbed on BA–TAP due to the abundant nitrogen atoms (denoted BA–TAP–Fe, Fig. 1a). As shown in SEM images, supramolecular BA–TAP–Fe was rod-like, with a length of *ca.* 30–300 μm and a diameter of *ca.* 1–5 μm (Fig. 1b), similar to BA–TAP (Fig. S2, ESI†). In sharp contrast, without any supramolecular preorganization of precursors, only inhomogeneous particles could be obtained by physical mixing, *e.g.*, *via* ball milling (denoted BA+TAP+Fe, Fig. 1c).

[a] *Jiangsu Engineering Laboratory of Smart Carbon-Rich Materials and Device, Jiangsu Province Hi-Tech Key Laboratory for Bio-Medical Research, School of Chemistry and Chemical Engineering, Southeast University, Nanjing 211189, China. E-mail: Yuanjian.Zhang@seu.edu.cn*
[b] *Medical School, Southeast University, Nanjing 210009, China*
[c] *Global Research Center for Environment and Energy Based on Nanomaterials Science (GREEN), National Institute for Materials Sciences (NIMS), 1-1 Namiki, Ibaraki, 305-0044, Japan*

† Electronic supplementary information (ESI) available. See DOI: 10.1039/c6cc09442b

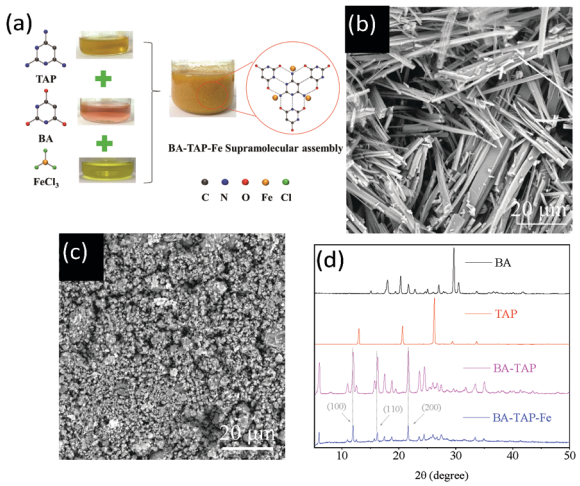

Fig. 1 The formation of a BA–TAP–Fe supramolecular precursor. (a) Photos and molecular structures of each precursor and the precipitated aggregate in aqueous solution after mixing. SEM images of (b) BA–TAP–Fe and (c) BA+TAP+Fe (prepared by ball-mill mixing of BA, TAP and $FeCl_3$). (d) XRD patterns of the BA, TAP, BA–TAP and BA–TAP–Fe showing the formation of a new crystalline structure by molecular assembling.

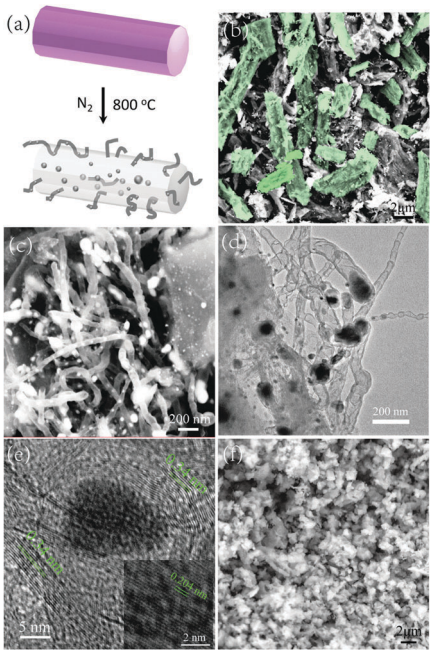

Fig. 2 The hierarchical structure of BA–TAP–Fe-800. (a) The preparation process of BA–TAP–Fe-800. SEM images of BA–TAP–Fe-800: (b) overview and (c) zoom-in showing more details of CNTs anchored on carbon rods. NB: Color scheme highlighting the rod structure. (d) TEM and (e) HRTEM images of BA–TAP–Fe-800. The inset in (e) shows the enlarged HRTEM image for the encapsulated nanoparticle. (f) SEM image of BA+TAP+Fe-800 (prepared by ball-mill mixing of BA, TAP and $FeCl_3$ and pyrolysis).

The formation of these regular rods may be directly related to the supramolecular preorganization between BA and TAP. The crystallinity of the BA–TAP–Fe was characterized by X-ray diffraction (XRD). The appearance of completely new peaks for BA–TAP and BA–TAP–Fe, compared to individual BA and TAP, was strong evidence for the creation of a new arrangement. The new peaks at 11.98, 16.26, and 21.68° for BA–TAP, most probably, were indexed to (100), (110), and (200) of the in-plane packing, respectively, according to analogous assembly of melamine and cyanuric acid.[4a,5] Moreover, after assembling, the C=O stretching vibration of BA in the FT-IR spectra (Fig. S3, ESI†) was shifted to a lower wavenumber from 1678 to 1598 cm^{-1}, and the NH_2 stretching vibration of TAP at 3456 and 3415 cm^{-1} was shifted to a broad peak at 3340 cm^{-1}, in agreement with previous reports.[4a,5] In addition, the homogeneous incorporation of $FeCl_3$ (Fig. S4, ESI†) did not cause significant changes in the morphology (Fig. 1b and Fig. S2, ESI†), the hydrogen bond between BA and TAP (Fig. S3, ESI†), and the crystalline structure (Fig. 1d). Nevertheless, BA–TAP–Fe showed a decrease of XRD intensity with respect to BA–TAP, implying that $FeCl_3$ was squeezed into the BA–TAP skeleton and induced a slight structural deformation.

It was noted that the surface area of BA–TAP–Fe was measured to be 5.3 $m^2\ g^{-1}$ and no predominated pore size distribution ranging from 1 to 70 nm was observed (Fig. S7a, ESI†), indicating that hydrogen bond-driven molecular assembly formed an ordered and close-packed crystalline structure. In contrast to MOFs that generally are microporous and have surface areas up to several thousand $m^2\ g^{-1}$, the hydrogen bond-driven assembly may avoid the collapse of the structure during further pyrolysis and achieve a high degree of graphitization and a porous structure that are desired for electrochemical catalysis.

Interestingly, after pyrolysis at 800 °C, the as-obtained BA–TAP–Fe-800 (Fig. 2b) largely retained the rod morphology of the BA–TAP–Fe supramolecular precursor without significant collapse of its original morphology, highlighting the importance of the ordered and close-packed crystalline structure formed by hydrogen bond-driven supramolecular assembly. As shown by the SEM (Fig. 2c) and TEM (Fig. 2d) images, a few CNTs with lengths of *ca.* 1–2 μm and diameters of *ca.* 40–100 nm that were wrapped in the carbon rod were observed. Such a hierarchical structure is expected to facilitate the transport of relevant species in electrocatalytic reactions and enhance the accessibility of catalytic sites.[5a] In addition, the nanoparticles were also identified in both carbon rods and CNTs (Fig. 2b–d). The high-resolution TEM image in Fig. 2e revealed that these nanoparticles showed a high degree of crystallization with a lattice distance of 0.204 nm, presumably attributed to the (220) planes of Fe_3C or the (110) planes of cubic Fe,[6] and wrapped with highly graphitic carbon composed of few graphite layers. It should also be noted that the formation of such long CNT-grafted carbon rods which made such carbon materials more graphitic (for more details see Fig. S6, ESI†) was a very rare example, and supposed to be useful for energy conversion applications.[3a,b,6b] For comparison, control samples without supramolecular preorganization, *e.g.*, those that contained only binary components including BA–Fe-800 and TAP–Fe-800 and that consisted of triple components but obtained *via* ball-mill mixing (BA+TAP+Fe-800), led to CNT-free carbon materials (Fig. 2f and Fig. S5, ESI†).

Fig. 3a shows the XRD pattern of BA–TAP–Fe-800 with a peak at 26.0°, which originated from the (002) planes of graphitic carbon rods and CNTs. In addition, the peaks at 43.7°, 44.7° and 65.0° could be indexed to the reflections from (102) planes of

Fe_3C (cementite, JCPDS No. 35-0772), and the (110) and (200) planes of cubic Fe (JCPDS No. 06-0696), respectively. It indicated that multiphase-Fe and graphitic carbon coexisted in BA–TAP–Fe-800, consistent with the TEM image in Fig. 2e. In contrast, the XRD pattern of the comparative samples without supramolecular preorganization (*i.e.* BA+TAP+Fe-800) showed only a broad peak at 26.1°, indicating a much poorer degree of graphitization, in agreement with the higher intensity ratio of the D-band to the G-band (I_D/I_G) in Raman spectra (Fig. S6, ESI†).[7]

The surface area and porosity of BA–TAP–Fe-800 were assessed using N_2 sorption isotherms (Fig. 3b). The pronounced hysteresis loop and pore size analysis by the density functional theory (DFT) method confirmed a narrow mesopore distribution (~4.1 nm, Fig. S7b, ESI†), which might have originated from the evaporation of Fe during heat treatment and the stacking of the nanocarbon.[3c,7b] The surface area estimated by the Brunauer–Emmett–Teller (BET) method was 232 $m^2\ g^{-1}$. Such a mesoporous structure and high surface area were favorable for active site exposure and rapid electrocatalytic reaction-relevant mass transportation. In contrast, BA+TAP+Fe-800 did not show such porosity, and the specific surface area was only 6.5 $m^2\ g^{-1}$ (Fig. S7c, ESI†). These results clearly demonstrated that supramolecular preorganization of precursors was crucial for the formation of carbon-based materials with a high degree of graphitization and a preferred pore structure.

The bonding configurations of BA–TAP–Fe-800 were investigated by X-ray photoelectron spectroscopy (XPS). The N1s spectra could be deconvoluted into four peaks at 398.4, 399.9, 401.0, and 402.7 eV, assignable to pyridinic N, pyrrolic N, graphitic N, and oxidized N, respectively (Fig. 3c).[7c,8] Pyridinic N should also include a contribution from nitrogen bound to iron (N–Fe), due to a small difference between the binding energies of pyridinic N and N–Fe.[6a,c] Pyridinic N, pyrrolic N, and graphitic N were all reported to play a crucial role in the electrocatalytic reaction,[6c,7c] and pyridinic N and pyrrolic N can interact with Fe, resulting in an Fe–N_x configuration.[7c] The high-resolution XPS spectra of Fe revealed Fe $2p_{3/2}$ peaks at 711.8 and 714.2 eV, and Fe $2p_{1/2}$ peaks at 723.4 and 727.4 eV, suggestive of the presence of zero-valence Fe (metallic iron or carbide) and Fe ions coordinated to N (Fe–N).[6a,c,7c] As we will discuss below, the coexistence of multiphase-Fe on the hierarchical N-doped graphitic carbon was essential to the electrocatalytic activities for BA–TAP–Fe-800. Therefore, BA–TAP–Fe-800 with a unique structure of multiphase-Fe anchored on hierarchical N-doped graphitic carbon was successfully prepared, exclusively by the supramolecular preorganization of the precursors *via* mixing monomers at the molecular level.

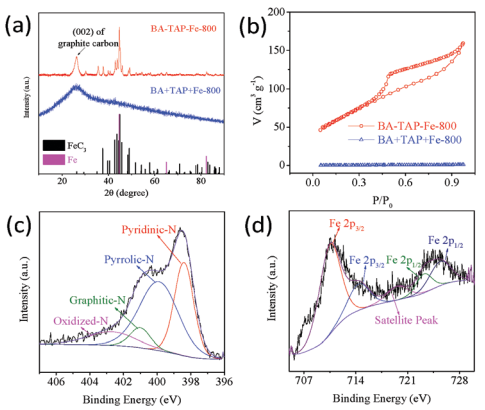

Fig. 3 (a) XRD patterns and (b) N_2 sorption isotherms of the BA–TAP–Fe-800 and BA+TAP+Fe-800. (c) C1s and (d) N1s XPS spectra of the BA–TAP–Fe-800.

Interestingly, the obtained BA–TAP–Fe-800 exhibited unusual trifunctional electrocatalytic activity for the ORR, OER and HER (Fig. 4), which was supposed to simplify the system and lower the cost associated with separate equipment and processes for different catalysts.[3a,b,5b,9] With respect to the counterparts (*i.e.*, BA–Fe-800, TAP–Fe-800 and BA+TAP+Fe-800) without supramolecular preorganization, BA–TAP–Fe-800 showed much higher electrocatalytic activities in all parameters such as the onset/half wave potential and kinetic current, highlighting the importance of supramolecular pre-arrangement of precursors for carbon-based electrocatalysts with a well-defined structure and composition for highly efficient activity.

More strikingly, BA–TAP–Fe-800 also showed impressive electrocatalytic performance that even surpassed Pt/C and RuO_2 in several key performance parameters (Table S1, ESI†). As shown in Fig. 4a, BA–TAP–Fe-800 had higher ORR activity than that of Pt/C in terms of the onset potential and half-wave potential as well as diffusion-limited current density. As far as we are aware, this is one of the few carbon-based catalysts with

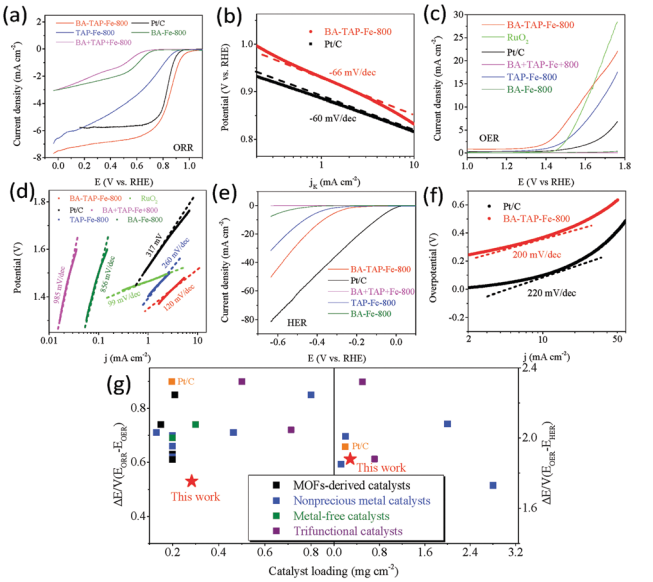

Fig. 4 Trifunctional electrocatalytic activities of BA–TAP–Fe-800. (a) Linear scan voltammogram curves of BA–TAP–Fe-800 and control samples in O_2-saturated solution for the (b) ORR and (c) OER and (e) HER in N_2-saturated solution. The Tafel curves of BA–TAP–Fe-800 and control samples for the ORR (b), OER (d) and HER (f). Electrolyte: 0.1 M KOH, scanning rate: 10 mV s^{-1}. Rotation speed: 1600 rpm. (g) Electrocatalytic activity of BA–TAP–Fe-800 compared with the literature values of other bi/trifunctional electrocatalysts evaluated by the difference of OER and ORR metrics ($\Delta E = E_{OER/j=10} - E_{ORR}$/onset) and HER and OER metrics ($\Delta E = E_{OER/j=10} - E_{HER/j=10}$). Detailed activity values are given in Table S1 (ESI†).

a more positive onset potential than that of Pt/C (Table S2, ESI†). The Tafel slope of BA−TAP−Fe-800 for the ORR was found to be *ca.* −66 mV per decade, which was similar to that of the Pt/C catalyst (Fig. 4b). In addition, the BA−TAP−Fe-800 catalyst showed an electron transfer number of ∼3.90 (Fig. S10, ESI†), a better tolerance to the methanol crossover effect (Fig. S11a, ESI†) and better long-term durability than the Pt/C catalyst (Fig. S11b, ESI†). For the catalytic OER, BA−TAP−Fe-800 had an onset potential of 1.36 V and a current density of 10 mA cm^{-2} at a potential of 1.55 V, superior to those of the state-of-art Pt/C electrode and RuO_2 nanoparticles (Fig. 4c and Table S1, ESI†). It is important to note that the OER activity of BA−TAP−Fe-800 outperformed previously reported metal-free OER catalysts and transition metal oxides, among the highest performances for the OER reported so far (Table S3, ESI†). Moreover, the Tafel slope of the BA−TAP−Fe-800 was 88 mV dec^{-1} which was lowest compared to their counterparts without using supramolecular preorganization (Fig. 4d), suggesting the best reaction kinetics for oxygen evolution again. The HER polarization curve of BA−TAP−Fe-800 depicted a potential of 0.33 V to achieve a current density of 10 mA cm^{-2} (Fig. 4e), comparable to those of the well-developed nanostructured MoS_2-based metallic catalysts and metal-free HER catalysts.[10] Although a higher overpotential of BA−TAP−Fe-800 was observed with respect to that of the Pt/C, the remarkable HER catalytic activity of BA−TAP−Fe-800 was evidenced by the rapid current increase with the potential. Such a trend can be observed by the lower Tafel slope for BA−TAP−Fe-800 (200 mV dec^{-1}) with respect to Pt/C (220 mV dec^{-1}) in the high current density region in Fig. 4f. Therefore, BA−TAP−Fe-800 was a highly efficient, non-precious trifunctional electrocatalyst for the ORR, HER and OER. Fig. 4g shows the electrocatalytic activity of BA−TAP−Fe-800 compared to those of reported bifunctional electrocatalysts in recent two years, which were evaluated by the difference of OER and ORR metrics ($\Delta E = E_{OER/j=10} - E_{ORR/onset}$) and HER and OER metrics ($\Delta E = E_{OER/j=10} - E_{HER/j=10}$). BA−TAP−Fe-800 exhibits a ΔE value of 0.53 V and 1.88 V, lower than those of the recently reported highly active bi/tri-functional electrocatalysts, corroborating the excellent trifunctional electrocatalytic nature of BA−TAP−Fe-800 (for more detailed comparison with those of the reported bi/tri-functional electrocatalysts in recent two years see Table S1, ESI†). To further understand the nature of the catalytic sites, two control experiments were carried out (for more details see Fig. S14, ESI†), which revealed that the coexistence of multiphase-Fe on the hierarchical N-doped graphitic carbon was essential to the outstanding ORR, OER and HER electrocatalytic activities.

In summary, a simple method for synthesizing trifunctional electrocatalysts was successfully developed by pyrolysis of supramolecular precursors. The close-packed crystalline structure of precursors after supramolecular assembling overcame the unwanted collapse during pyrolysis of other assembly precursors such as MOFs, making the final catalysts with multiphase-Fe anchoring on hierarchical N-doped graphitic carbon. As a result, the obtained catalysts showed superior catalytic performance for the ORR, OER and HER compared to their counterparts without any precursor preorganization. With the tunable compositions and morphologies of supramolecular hydrogen bond-driven assembly, this work showed the potential to design advanced task-specific multifunctional catalysts as a replacement for expensive metals for sustainable electrochemical energy storage and conversion. Work focusing on the relationship between specific structures and electrocatalytic activity is ongoing.

This work was supported by the National Natural Science Foundation of China (91333110, 21675022), the Natural Science Foundation of Jiangsu Province (BK20160028), and the Fundamental Research Funds for the Central Universities.

Notes and references

1 (*a*) M. Shalom, S. Inal, C. Fettkenhauer, D. Neher and M. Antonietti, *J. Am. Chem. Soc.*, 2013, **135**, 7118–7121; (*b*) M. R. Molla, P. Prasad and S. Thayumanavan, *J. Am. Chem. Soc.*, 2015, **137**, 7286–7289.
2 (*a*) P. Pachfule, D. Shinde, M. Majumder and Q. Xu, *Nat. Chem.*, 2016, **8**, 718–724; (*b*) X. Long, G. Li, Z. Wang, H. Zhu, T. Zhang, S. Xiao, W. Guo and S. Yang, *J. Am. Chem. Soc.*, 2015, **137**, 11900–11903.
3 (*a*) A. Aijaz, J. Masa, C. Rösler, W. Xia, P. Weide, A. J. R. Botz, R. A. Fischer, W. Schuhmann and M. Muhler, *Angew. Chem., Int. Ed.*, 2016, **55**, 4087–4091; (*b*) B. Y. Xia, Y. Yan, N. Li, H. B. Wu, X. W. Lou and X. Wang, *Nat. Energy*, 2016, **1**, 15006; (*c*) H. Zhong, J. Wang, Y. Zhang, W. Xu, W. Xing, D. Xu, Y. Zhang and X. Zhang, *Angew. Chem., Int. Ed.*, 2014, **53**, 14235–14239; (*d*) J. Wei, Y. Liang, Y. Hu, B. Kong, J. Zhang, Q. Gu, Y. Tong, X. Wang, S. P. Jiang and H. Wang, *Angew. Chem., Int. Ed.*, 2016, **55**, 12470–12474; (*e*) S. Dou, X. Li, L. Tao, J. Huo and S. Wang, *Chem. Commun.*, 2016, **52**, 9727–9730.
4 (*a*) Y. S. Jun, E. Z. Lee, X. Wang, W. H. Hong, G. D. Stucky and A. Thomas, *Adv. Funct. Mater.*, 2013, **23**, 3661–3667; (*b*) Y.-S. Jun, J. Park, S. U. Lee, A. Thomas, W. H. Hong and G. D. Stucky, *Angew. Chem., Int. Ed.*, 2013, **125**, 11289–11293.
5 (*a*) S. Guo, Z. Deng, M. Li, B. Jiang, C. Tian, Q. Pan and H. Fu, *Angew. Chem., Int. Ed.*, 2016, **128**, 1862–1866; (*b*) J. Zhang, L. Qu, G. Shi, J. Liu, J. Chen and L. Dai, *Angew. Chem., Int. Ed.*, 2016, **55**, 2230–2234.
6 (*a*) W. Jiang, L. Gu, L. Li, Y. Zhang, X. Zhang, L. Zhang, J. Wang, J. Hu, Z. Wei and L. Wan, *J. Am. Chem. Soc.*, 2016, **138**, 3570–3578; (*b*) W. Yang, X. Liu, X. Yue, J. Jia and S. Guo, *J. Am. Chem. Soc.*, 2015, **137**, 1436–1439; (*c*) Z. Wu, X. Xu, B. Hu, H. Liang, Y. Lin, L. Chen and S. Yu, *Angew. Chem., Int. Ed.*, 2015, **54**, 8179–8183.
7 (*a*) W. Ding, L. Li, K. Xiong, Y. Wang, W. Li, Y. Nie, S. Chen, X. Qi and Z. Wei, *J. Am. Chem. Soc.*, 2015, **137**, 5414–5420; (*b*) H.-W. Liang, W. Wei, Z.-S. Wu, X. Feng and K. Müllen, *J. Am. Chem. Soc.*, 2013, **135**, 16002–16005; (*c*) L. Lin, Q. Zhu and A.-W. Xu, *J. Am. Chem. Soc.*, 2014, **136**, 11027–11033.
8 (*a*) F. Meng, Z. Wang, H. Zhong, J. Wang, J. Yan and X. Zhang, *Adv. Mater.*, 2016, **28**, 7948–7955; (*b*) X. Cui, S. Yang, X. Yan, J. Leng, S. Shuang, P. M. Ajayan and Z. Zhang, *Adv. Funct. Mater.*, 2016, **26**, 5708–5717; (*c*) D. Yan, S. Dou, L. Tao, Z. Liu, Z. Liu, J. Huo and S. Wang, *J. Mater. Chem. A*, 2016, **4**, 13726–13730.
9 (*a*) J. Li, Y. Wang, T. Zhou, H. Zhang, X. Sun, J. Tang, L. Zhang, A. M. Al-Enizi, Z. Yang and G. Zheng, *J. Am. Chem. Soc.*, 2015, **137**, 14305–14312; (*b*) H. Jin, J. Wang, D. Su, Z. Wei, Z. Pang and Y. Wang, *J. Am. Chem. Soc.*, 2015, **137**, 2688–2694; (*c*) C. Tang, N. Cheng, Z. Pu, W. Xing and X. Sun, *Angew. Chem., Int. Ed.*, 2015, **54**, 9351–9355.
10 (*a*) Y. Li, H. Wang, L. Xie, Y. Liang, G. Hong and H. Dai, *J. Am. Chem. Soc.*, 2011, **133**, 7296–7299; (*b*) Y. Zheng, Y. Jiao, Y. Zhu, L. H. Li, Y. Han, Y. Chen, A. Du, M. Jaroniec and S. Z. Qiao, *Nat. Commun.*, 2014, **5**, 3783.